

# Combined fluid-dynamic modelling of hybrid rocket internal ballistics and nozzle heat transfer

*G.D. Di Martino\*, S. Mungiguerra\*, C. Carmicino\* and R. Savino\**

*\*Università di Napoli "Federico II"*

*80125 Napoli, Italy*

## Abstract

A computational thermo-fluid-dynamic model of the hybrid rocket internal ballistics has been developed in the present work. Numerical simulations of the flowfield in a laboratory 200 N-class hybrid rocket engine, operated with gaseous oxygen and high-density polyethylene or acrylonitrile-butadiene-styrene have been carried out. The objective is twofold: first the prediction of the solid fuel regression rate, which is calculated with an improved gas/surface interface treatment based on local mass, energy and mean mixture fraction balances as well as proper turbulence boundary conditions, along with chamber pressure and combustion efficiency. Second, the detailed study of the discharge nozzle flow and heat transfer. For the validation of the model, data retrieved from two firing tests are compared with the numerical results revealing good agreement of the average regression rates, fuel consumption axial profiles, and of the chamber pressure and combustion efficiency. The output of the motor ballistic simulations are then used for a detailed numerical study of the flow through the nozzle and of the unsteady thermal field inside the nozzle solid block showing different behaviours of graphite compared to ceramic material nozzle, highlighting the severe thermal gradient occurring in the ceramic material.

## 1. Introduction

Hybrid rockets are chemical propulsion engines employing propellants in two separate phases. In the classical system arrangement, namely, the fuel is stored in the combustion chamber in the solid state and a gaseous or liquid oxidizer is properly injected in a port obtained in the solid fuel grain. Usually a forward dump plenum, upstream of the solid grain, and an aft-mixing chamber thermally shielded are employed. Rocket performance is governed by the rate at which the fuel is gasified, i.e. by the fuel regression rate, as this latter determines the total mass flow rate and the overall oxidizer-to-fuel mixture ratio, which, for a given chamber pressure, control the motor thrust and the ideal specific impulse. For a given fuel, regression rate is basically limited by the heat flux input to the solid grain, which mainly depends on the thermo-fluid dynamics in the combustion chamber. This latter is significantly influenced by several geometrical parameters, such as, among the others, the oxidizer injection configuration. Internal ballistic calculations based on the classical boundary-layer theory [1], even when applied to simple engine arrangements, in which a head-end injector is set up and an axial mean flow is established in the fuel port, can fail to predict the actual motor performance for the lack of the oxidizer-injection fluid dynamics modelling [2, 3], especially for low aspect-ratio motors. Hence, a fundamental task is the prediction and/or the reproduction of the motor internal ballistics. Another challenge for the hybrid rocket technology development is the optimization of the design of thermal insulations. The inner surface of the exhaust nozzle, through which the flow is accelerated to supersonic conditions producing the required thrust, is the most critical in this sense, as it is subjected to the highest shear stress and heat fluxes in a chemically aggressive environment. These severe conditions usually lead to removal of surface material (ablation) due to heterogeneous reactions between oxidizing species in the hot gas and the solid wall. Because of the material erosion, there is an enlargement of the nozzle throat section and a consequent decrease of rocket thrust, with detrimental effects over the motor operation. Thus, the requirement that dimensional stability of the nozzle throat should be maintained makes the selection of suitable rocket nozzle materials extremely hard. In recent years, Ultra-High Temperature Ceramics (UHTC) have been extensively investigated as innovative materials for rocket application, but, although their outstanding erosion resistance, they yield poor thermal shock resistance and damage tolerance, which can lead to catastrophic failure [4]. For this reason, new reinforced UHTC systems have been conceived by incorporating high aspect-ratio secondary phases, mainly silicon carbide (SiC) whiskers, carbon (C) or silicon carbide fibres [5]. Prototypes of this new class of materials have to be designed and characterized in firing tests. Experimental testing along with computational fluid dynamic (CFD) simulations are, thus, both needed to improve the design and

the current performance prediction capabilities of such propulsion systems. In this framework, the University of Naples is involved in the European project C<sup>3</sup>HARME – Next Generation Ceramic Composites for Combustion Harsh Environment and Space, in collaboration with other research centres, universities and industries.

CFD modelling of the flowfield in the combustion chamber of a hybrid propellant rocket has been the subject of considerable interest recently (for instance see Ref. [6, 7, 8, 9, 10]), but, for the huge computational cost and very challenging task, comprehensive models to describe the complex interactions among fluid dynamics [11], solid fuel pyrolysis [12], oxidizer atomization and vaporization, mixing and combustion in the gas phase [13], nozzle thermochemical erosion [14], particulate formation, and radiative characteristics of the flame [9, 15] are still lacking, and numerical simulations are rather considered as a qualitative tool to afford the thermo-fluid-dynamics of the rocket. A research effort is definitely of major importance in order to change this trend, by obtaining quantitatively accurate results.

In Ref. [16] the authors preliminarily defined a simplified numerical model apt to simulate the thermo-fluid-dynamic field in a hybrid rocket in which the fuel regression rate was an assigned parameter, with the main purpose of screening several oxidizer injectors based on the resulting motor performance. That model has been successively improved, by including the interaction between the gaseous flowfield and the solid fuel surface pyrolysis to derive the regression rate along the fuel grain and transient numerical simulations have been carried out by updating the fuel port shape during the engine run to capture the post-burn fuel axial consumption profile [17]. In the current paper, the model has been further elaborated with an improvement of the gas/surface interface treatment based on local mass, energy and mean mixture fraction balances as well as with the application of a proper turbulence boundary condition. Furthermore, the computational domain has been here extended to include the aft-mixing chamber and the discharge nozzle, which allowed for the computation of the chamber pressure (which in the previous works was an input to the problem) and the estimation of the combustion efficiency.

The main idea behind the study presented here was to split the computational analysis of the whole motor internal ballistics, including the nozzle, from a dedicated investigation into the nozzle itself. Thus, for a detailed thermal analysis of the nozzle material behaviour, a combination of CFD simulations of the rocket ballistics with the ones of the reacting flowfield across the exhaust nozzle, have been carried out with proper matching conditions.

With the aim of validating the internal ballistics computational model, two test cases are considered in the following; they differ for the solid fuel, which in one case was High-Density Polyethylene (HDPE) and, in the other, Acrylonitrile-Butadiene-Styrene (ABS); both fuels were burned with gaseous oxygen. After that, a refined unsteady fluid/solid coupled simulation has been performed on the nozzle only, by employing the results of the previous calculation as boundary condition.

## 2. Experimental Rig and Test Cases Description

The test rig is a versatile set up primarily designed for testing hybrid rocket engines of several sizes [18]. It is equipped with a test bench and a general-purpose acquisition system, which allow evaluating propellant performance and combustion stability [19], testing of sub-components and/or complete power systems, nozzles [20], air intakes, catalytic devices [21], burners, ignition and cooling systems [4, 22].

### 2.1 Lab-scaled Rocket and Test Facility

The small-scale lab rocket used for the tests presented in the paper, and the test stand are described in this section. The layout of the rocket engine is depicted in Figure 1, and a schematic of the test facility is shown in Figure 2.

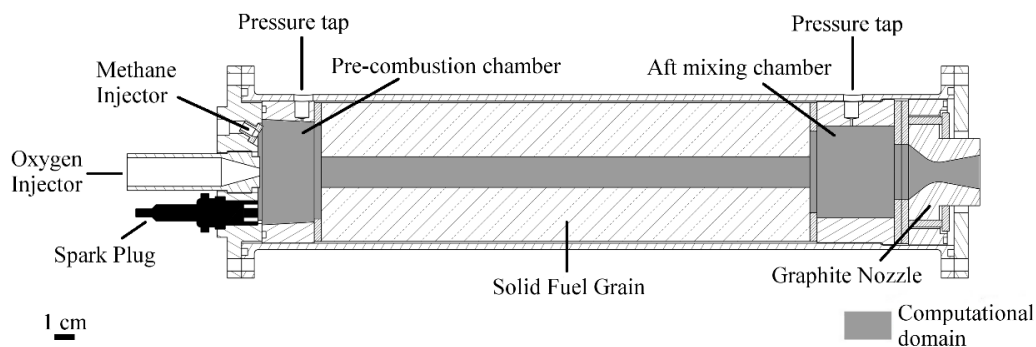


Figure 1: Motor layout and computational domain

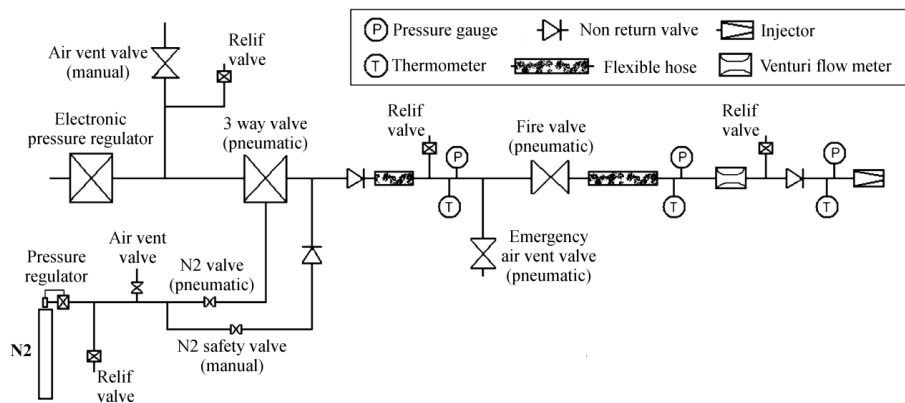


Figure 2: Test facility schematic

Gaseous oxygen is supplied by a reservoir of 4 cylinders that is connected to the motor feed line with a TESCOM electronically controlled pressure valve. Mass flow rate is evaluated through gas temperature and pressure measurements upstream of the throat of a choked Venturi tube. Nitrogen is purged into the chamber for the burn out and in case of an emergency shutdown.

The lab-scale rocket has an axisymmetric combustion chamber, with 350-mm length and 69-mm case inner diameter. The tests presented in the following sections have been performed with a converging nozzle injector, whose exit-section diameter is 6 mm, which delivered oxygen in single-port cylindrical fuel grains of either HDPE or ABS.

Upstream and downstream of the solid grain a dump plenum and an aft-mixing chamber are set up, respectively.

A graphite converging-diverging exhaust nozzle has been employed. The graphite nozzle can be easily replaced by segmented nozzles with UHTC (or other materials) throat insert or by complete ceramic nozzles for the next step of the study.

Chamber pressure is measured by means of two Setra C206 transducers, which are set up in the prechamber and in the aft-mixing chamber. Methane is injected for 3 seconds simultaneously with oxygen in the prechamber where a spark plug, powered by a Honeywell solid-state igniter spark generator, is arranged to ignite the motor.

All the analog signals are sampled at 5 kHz, digitally converted, processed and recorded on the hard disk by a National Instruments PXI Express standard system wired with the computer by means of optical fibre cables. Acquired signals are stored in binary format (for post-processing) and, after a downsampling to 100 Hz with a boxcar average, in text format for a quick visualization. All the diagrams presented in the next sections will show downsampled data.

## 2.2 Firing Test Cases

Two firing tests with different polymeric fuels are considered as test cases for the validation of the numerical models. The first test (Test 1) was performed with HDPE fuel grain whose length was equal to  $L = 220\text{mm}$  and the initial port diameter was equal to  $D_0 = 15\text{mm}$ . The second test (Test 2) was performed with an ABS fuel grain whose length was equal to  $L = 240\text{mm}$  and the initial port diameter was equal to  $D_0 = 15\text{mm}$ . The different grain lengths were compensated with different postchambers.

The test duration was set to 12 s in both tests. A picture of the rocket exhaust plume for the firing test with HDPE is shown in Figure 3; Figure 4 shows a sequence of pictures of the rocket nozzle taken at three instants after the engine burnout, from the brightness one can see that very high temperatures in the nozzle back are reached at the end of the test.



Figure 3: Rocket exhaust plume (Test 1 with HDPE)

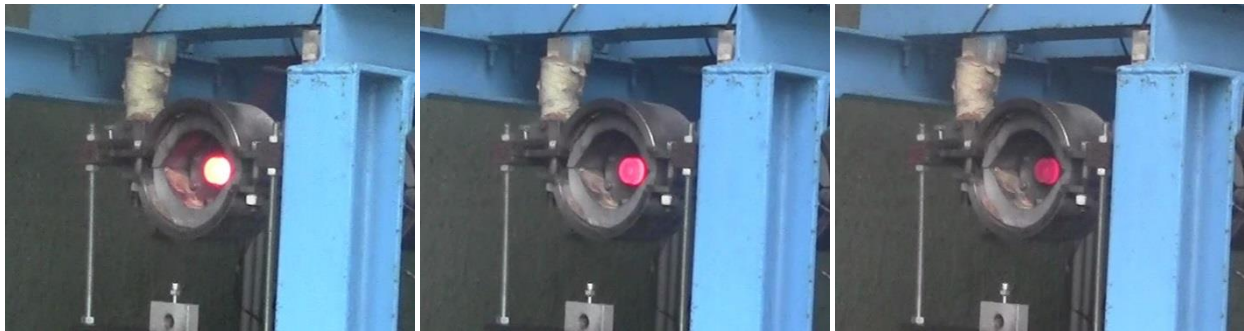


Figure 4: Sequence of pictures of the hybrid rocket exhaust nozzle after the firing test (Test 1 with HDPE)

The trend of the motor operating pressures over the firing time is shown in Figure 5 for the two tests.

Referring to Test1, the oxygen feeding valve starts to open at 0 s (test initial time) to deliver the oxygen flowrate targeted for the test; for the valve opening delay, oxygen starts flowing after about 0.9 s and stops after 12.3 s; simultaneously high-pressure nitrogen is fed into the engine for immediate shutdown. The decreasing trend of the chamber pressure in Test 1 can be explained with the nozzle erosion during the test, whose throat diameter has increased from 9.6 mm to 10.6 mm as measured after the test. The nozzle throat diameter in Test 2 was equal to 12 mm and no significant erosion was detected.

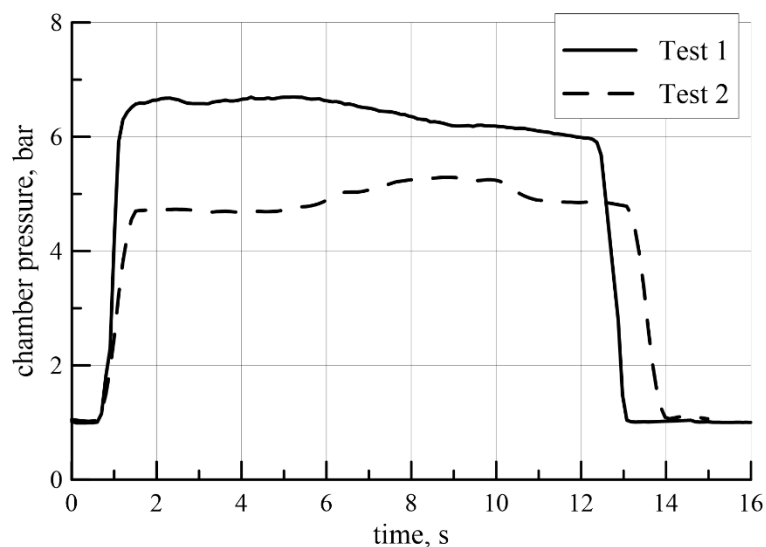


Figure 5: Operating pressures vs time

The average parameters measured over the firings are summarised in Table 1. The mass loss method [23] has been used to calculate the average values starting from the measurement of the burned fuel mass and burning time, which is determined from the pressure-time trace as the period from the inflection point on the first main rise portion of the prechamber pressure signal and the one on the decrease phase after the oxygen valve closure [2]. Finally, the local time-averaged regression rate can be estimated as follows

$$\bar{r} = \frac{D_{2x} - D_1}{2t_b} \quad (1)$$

in which  $D_{2x}$  is the local inner grain diameter measured with a caliper after sectioning the after-burn grain in the axial direction,  $D_1$  is the grain port initial diameter and  $t_b$  is the burning time.

Table 1: Firing test operating conditions

Parameter	Test 1	Test 2
Fuel	HDPE	ABS
Time-averaged oxygen mass flow rate, g/s	27	27.5
Initial port diameter, mm	15	15
Time-space averaged fuel mass flow rate, g/s	4.8	10.5
Time-space averaged regression rate, mm/s	0.39	0.61
Time-averaged aft-chamber pressure, atm	6.41	4.78
Time-averaged overall mixture ratio	5.63	2.62
Postburn space-averaged port diameter, mm	23.8	28.4
Time-space-averaged port diameter, mm	19.4	22.4

### 3. Physical and Numerical Model

#### 3.1 Hybrid rocket internal ballistics thermo-fluid dynamic modelling

The main goal of the CFD simulations presented in this paper is the determination of the local fuel regression rate. Numerical simulations are carried out with a commercial fluid dynamic solver with ad-hoc user-defined functions. The RANS equations for single-phase multicomponent turbulent reacting flows are solved with a control-volume-based technique and a pressure-based algorithm [24].

The Shear Stress Transport (SST) turbulence model [25] has been employed for its improved capability of predicting flows with separated regions. This latter is a combination of the robust and accurate  $k-\omega$  model, developed by Wilcox [26], in the near-wall region, with the standard  $k-\varepsilon$  model implemented away from the wall using a blending function. Assuming that the chemical kinetics is fast compared to the diffusion processes occurring in the motor for the typical mass fluxes and chamber pressures considered here [27], the non-premixed combustion of oxygen and the gaseous fuel injected from the grain wall is modelled by means of the Probability Density Function (PDF) approach coupled to chemical equilibrium [28]. Accordingly, combustion is simplified to a mixing problem (mixed is burnt), and the difficulties associated with closing non-linear reaction rates are avoided. The turbulence-chemistry interactions are described by means of the average mixture fraction,  $f$ , and its variance. The shape of the assumed PDF is described by the  $\beta$ -function of the mean mixture fraction and its variance [29]. Once  $\tilde{f}$  and  $\tilde{f'^2}$  are calculated at each point in the flowfield, the known PDF is used to compute the time-averaged values of individual species mole fractions, density, and temperature with simple thermochemistry calculations based on the minimization of Gibbs free energy [30]. Ethylene has been considered as gaseous fuel at the wall in the test case with HDPE, while an empirical mixture defined according to Ref. [31] has been considered in the test case with ABS.

Heat capacities, molecular weights, and enthalpies of formation for each species considered are extracted from the solver chemical database; the specific heat is determined via the mixing law. Molecular dynamic viscosities and thermal conductivities of each species are calculated as functions of local temperature, according to Ref. [30].

The typical computational domain is shown in Figure 6, representing the internal volume of the prechamber, the fuel grain, the post-chamber and the nozzle, shaded in grey in Figure 1. The main dimensions are listed in Table 2. Note that the one represented in Figure 6 is only an example, inasmuch as the grain length and the port diameter change for the different considered cases.

On the inner surface of both the prechamber and postchamber as well as on the nozzle wall no-slip and adiabatic boundary conditions are imposed. At the injector exit section a mass flow boundary condition is prescribed along with

the temperature (equal to 300 K), the oxygen mass fraction and the turbulent quantities, while a pressure outlet condition is set at the nozzle exit section.

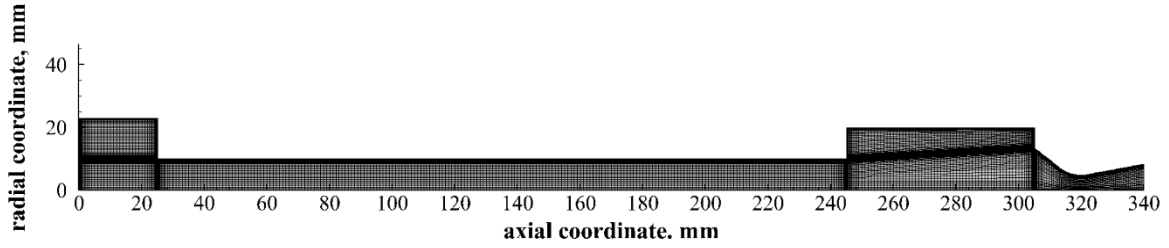


Figure 6: Typical computational grid for the simulation of hybrid rockets

Table 2: Computational domain dimensions

Prechamber diameter	Prechamber length	Fuel grain length	Fuel grain initial port diameter	Post-chamber diameter	Post-chamber length
46 mm	25 mm	220; 240 mm	15 mm	40 mm	60; 40 mm

### 3.1.1 Gas-solid Fuel Interface Modelling

The theoretical model formulation is completed by assigning the boundary conditions at the interface between the gaseous flow region and the solid fuel wall, which can properly describe the pyrolysis phenomenon. The fuel surface is, actually, an inlet boundary along which both the fuel mass flux, the temperature and the mixture fraction are unknown to be determined.

Under the hypothesis that no material is removed from the surface in a condensed phase (neither solid, such as in the case of fuel loaded with metal particles, nor liquid, when, for instance paraffin wax is used), the mass conservation at the gas-solid interface over a pyrolyzing fuel grain imposes that

$$(\rho v)_w = \rho_f \dot{r} \quad (2)$$

where  $\rho$  is the gas density at the wall, and  $v$  is the normal-to-wall velocity component due to the pyrolysis products injection;  $\rho_f$  is the solid fuel density and  $\dot{r}$  is the local regression rate.

The energy balance at the gas-solid interface, taking into account the convective heat transfer from the gas to the fuel surface, the heat conduction into the solid, and neglecting the radiation (the latter is known to produce second order effects with the non-metallized propellant considered here [32]) leads to the following relationship between the convective heat flux to the wall,  $\dot{q}_w$ , and the regression rate [3]

$$\dot{q}_w = \left( k_g \frac{\partial T}{\partial n} \right)_w = \rho_f \dot{r} [\Delta h_p + c_f (T_w - T_{wi})] \quad (3)$$

where  $n$  is the coordinate normal to surface oriented from solid to gas,  $k_g$  the gas thermal conductivity,  $c_f$  is the solid heat capacity per unit mass,  $\Delta h_p$  the so-called heat of pyrolysis,  $T_w$  is the fuel surface temperature, and  $T_{wi}$  is its initial temperature (which is assumed equal to the one of the external surface of the fuel). Usually, the term in brackets at the right-hand side is indicated with  $h_v = \Delta h_p + c_f (T_w - T_{wi})$ , and it represents the effective heat of gasification of the fuel, which, further than for the heat of pyrolysis, accounts for the heat conducted into the solid grain. Note that, concerning the latter energy term, for the negligible surface temperature axial variation (as will be observed next), heat conduction only in the direction normal to the grain surface is considered.

The fuel pyrolysis is, finally, modelled with the following semi-empirical Arrhenius-type equation [12] relating the regression rate to the fuel surface temperature

$$\dot{r} = A \cdot \exp\left(-\frac{E_a}{2RT_w}\right) \quad (4)$$

where  $A$  is the pre-exponential factor,  $E_a$  is the activation energy and  $R$  is the universal gas constant.

The values of the constants appearing in Eq. (3) and Eq. (4) considered for the HDPE and for ABS fuel grains analysed in this work are summarized in Table 3. Density, specific heat and heat of pyrolysis for HDPE are taken from the work in Ref. [33], while the values of the pre-exponential factor and the activation energy from Ref. [12] by modifying the activation energy to match the surface temperature commonly observed in polymeric hybrid fuels (which is around 800 K) [17, 34]. The properties for ABS are taken from the work in Ref. [35], with similar considerations for the activation energy.

Table 3: Solid fuels properties and rate constants

Fuel	Density, $\rho_f$ kg/m <sup>3</sup>	Specific heat, $c_f$ J/kg K	Heat of pyrolysis, $\Delta h_p$ MJ/kg	Initial fuel temperature, $T_{wi}$ K	Pre-exponential factor, $A$ mm/s	Activation Energy, $E_a$ , kJ/mol
HDPE	950	2833	4.045	300	$4.78 \cdot 10^6$	190
ABS	1020	2620	1.890	300	7.194	32

Once Eq. (3) and Eq. (4) are combined, given the heat flux to the wall from the flowfield solution, both the fuel surface temperature and the regression rate can be determined. As the flowfield, indeed, depends on both parameters at the fuel wall, an iterative procedure is needed for the problem solution.

A specific treatment of the boundary condition on the mean mixture fraction at the gas-solid interface is needed as well. In fact, for the low fuel regression rate of hybrid rockets, the normal convection of the fuel at the grain surface is relatively weak compared to the gas convection in the cells near the boundary; furthermore, there exist significant differences in the species concentrations between the fuel surface and the cells adjacent to the boundary, so that a steep mixture fraction gradient at the fuel wall is present. In this conditions the diffusive flux plays a dominant effect in the mixture fraction transport. As a consequence, if a simple Dirichlet-type boundary condition is applied on the gas-fuel interface, by imposing  $f = 1$ , extra mixture fraction will be diffused into the flow affecting the global oxidizer to fuel ratio and the chemical equilibrium properties, which eventually leads to an incorrect estimation of the characteristic exhaust velocity and chamber pressure.

A possible approach proposed to mitigate this problem may consist in imposing that the diffusion coefficient  $\mu_t/Sc_t$  is equal to zero in the cells close to the fuel inlet boundary, but this would imply a non-exact evaluation of the gradients in this zone, and, in particular, of the heat flux to the fuel wall, which, for Eq. (3), would lead to a mistaken regression rate.

The correct solution to this problem is to consider an additional equation for the mean mixture fraction balance at the gas-solid interface, which can be expressed as

$$(\rho v)_w f_w - \left( \frac{\mu_t}{Pr_t} \frac{\partial f}{\partial n} \right)_w = \rho_f \dot{r} \quad (5)$$

According to this equation, the total mass flux entering the gaseous domain due to the solid fuel regression, which appears on the right-hand side of the equation and represents the production term, is partially balanced by the convection and partially by the diffusion of the fuel mass fraction.

Note that Eq. (3), Eq. (4) and Eq. (5) constitute a system of three algebraic equations in the three unknowns regression rate, surface temperature and mixture fraction, which needs the computation of the flowfield at each iterative step to be solved.

Finally, the enhanced wall treatment is employed for the turbulence boundary conditions at the gas/solid interface.

### 3.2 Thermal analysis of solid nozzle

The numerical model described in the previous sections provides the required inlet boundary conditions for the detailed numerical analysis of the flowfield through the discharged nozzle, which is finally coupled with the thermal field in the nozzle bulk material. To this purpose the RANS equations with the SST  $k-\omega$  model as turbulence closure have been solved as well. However, a different model is preferable for the chemical species transport and reaction mechanism, as the chemical equilibrium hypothesis is no longer applicable for an accurate analysis of the fast accelerating flow through the nozzle. In fact, although the assumption of chemical equilibrium does not influence significantly the estimation of the chamber pressure and of the engine performance, it can affect the correct prediction of the chemical composition evolution and of the heat transfer to the wall. Accordingly, in this case the transport equations for the main combustion products (O<sub>2</sub>, C<sub>2</sub>H<sub>4</sub>, H<sub>2</sub>O, CO<sub>2</sub>, CO, H<sub>2</sub>, H, O, OH are the species considered in the current model) have been solved, and the Eddy Dissipation Concept (EDC) model [36] has been employed for the

combustion mechanism, which accounts for detailed chemical reaction rates in turbulent flows. Consequently, the Arrhenius rate  $K$  for each reaction is calculated as

$$K = AT^\beta \exp\left(-\frac{E_a}{RT}\right) \quad (6)$$

where the constants have been taken from Ref. [37] and are reported in Table 4. In this case the Discrete Ordinates model [38] for the radiation is included in the numerical modelling.

Table 4: C<sub>2</sub>H<sub>4</sub> – O<sub>2</sub> reaction system

No.	Reaction <sup>a</sup>	A <sup>b</sup>	$\beta$	E <sub>a</sub> <sup>b</sup>
1	C <sub>2</sub> H <sub>4</sub> + O <sub>2</sub> ⇌ 2CO + 2H <sub>2</sub>	1.80e+14	0.0	35500
2	CO + O ⇌ CO <sub>2</sub> + M	5.30e+13	0.0	-4540
3	CO + OH ⇌ CO <sub>2</sub> + M	4.40e+06	1.5	-740
4	H <sub>2</sub> + O <sub>2</sub> ⇌ OH + OH	1.70e+13	0.0	48000
5	H + O <sub>2</sub> ⇌ OH + O	2.60e+14	0.0	16800
6	OH + H <sub>2</sub> ⇌ H <sub>2</sub> O + H	2.20e+13	0.0	5150
7	O + H <sub>2</sub> ⇌ OH + H	1.80e+10	1.0	8900
8	OH + OH ⇌ H <sub>2</sub> O + O	6.30e+13	0.0	1090
9	H + H ⇌ H <sub>2</sub> + M	6.40e+17	-1.0	0
10	H + OH ⇌ H <sub>2</sub> O + M	2.2e+22	-2.0	0

<sup>a</sup>Third-body efficiencies for all thermolecular reactions are 2.5 for  $M = \text{H}_2$ , 16.0 for  $M = \text{H}_2\text{O}$ , and 1.0 for all other  $M$ .

<sup>b</sup>Units are in seconds, moles, cubic centimetres, calories and degree Kelvin

The last step of the numerical simulations is related to the thermal analysis of the solid nozzle block. In particular, the time-dependent temperature field inside the sample and its supporting elements can be computed solving the energy equation

$$(\rho C)_s \frac{\partial T}{\partial t} = \lambda_s \nabla^2 T \quad (7)$$

where  $\rho_s$ ,  $C_s$  and  $\lambda_s$  are the solid density, specific heat and thermal conductivity, respectively. The typical computational grid for the simulation of the flow field through the exhaust nozzle of the hybrid rocket is shown in Figure 7, where also the solid region for the thermal analysis is included.

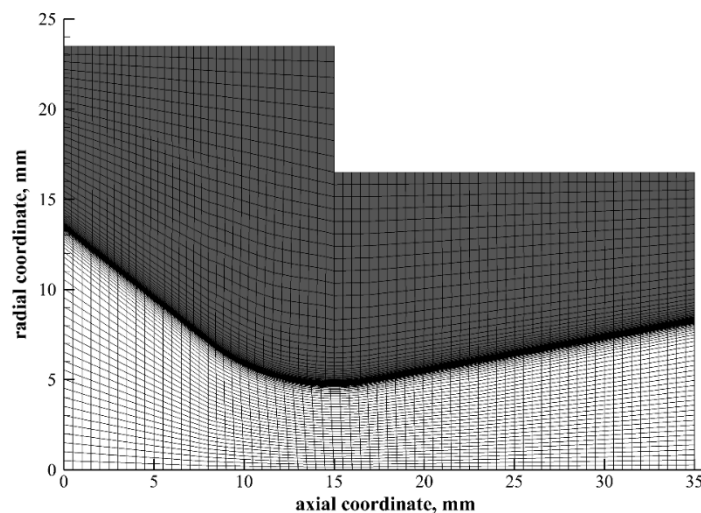


Figure 7: Typical computational grid for the simulation of the flow through the nozzle and the thermal field in the solid components

With reference to Figure 7, a pressure inlet boundary condition is set on the inlet section of the nozzle imposing the total pressure, the total temperature and the chemical composition profiles estimated by means of the model described in the previous section. A pressure outlet boundary condition is set at the exit section.

The thermal coupling condition is set on the interfaces between fluid and solid domains, that is temperature and heat flux continuities:

$$T_{f,int} = T_{s,int} \quad (8)$$

$$\lambda_f \frac{\partial T}{\partial n} \Big|_{f,int} = \lambda_s \frac{\partial T}{\partial n} \Big|_{s,int} \quad (9)$$

where  $n$  is the normal direction of the interface, the subscript  $f$  represents the fluid region, and  $s$  the solid one.

On the nozzle outer walls contained in the motor case an adiabatic boundary condition is imposed, whereas on the surface exposed to the atmosphere a radiative heat transfer with the environment is considered.

## 4. Numerical Results

In this section the numerical results obtained with the abovementioned method are presented. First, the results of the two simulations carried out in the cases of HDPE and ABS grains are presented and compared with the experimental data for the validation of the employed numerical model. After that, the results of the detailed CFD simulation of the flowfield through the rocket nozzle are shown. Finally, the results of the unsteady thermal analysis of the solid component in the two cases of a graphite nozzle and of a ceramic nozzle are discussed, highlighting the main differences in the two cases.

### 4.1 Numerical simulations of hybrid rocket internal ballistics

In this section, the results of the numerical simulations carried out in the conditions of the two test cases presented in Sec. 2.2 are analysed. Values of oxygen mass flow rate in Table 1 are enforced in the calculation. The simulations were carried out considering the time-spatially averaged grain port diameter in the burns, since they can provide meaningful details of the flowfield in the hybrid rocket combustion chamber and the corresponding average regression rate, and are then valuable for a preliminary validation of the numerical model.

Figure 8 a) and Figure 8 b) show the plots of the temperature contours calculated in the two test cases; on the top half of each picture the streamlines are overlapped, while the fuel mass fraction in the unburnt mixture isolines are drawn on the bottom halves.

First, as expected, the main results already found with the simplified models [16, 17] previously developed are here confirmed: the combustor inlet flowfields, which are similar in the two considered test cases, are dominated by the development of the oxygen jet emerging from the axial injector (that is clearly distinguishable from the low temperature region in Figure 8), which spreads almost linearly up to the impingement point on the grain surface. Upstream of the impingement point, in the entrance region of the grain, there is an extended recirculation region characterized by a main, broad counterclockwise-rotating vortex that is bounded, on the front side, by the zone of oxygen impingement. In the pre-combustion chamber, another large vortex, clockwise rotating, is formed delimiting the main one on the backside. Finally, also in the aft-mixing chamber, a large trapped counterclockwise-rotating vortex is formed [39, 40], which further promotes the propellant mixing, improving the combustion efficiency.

As a result of the flow recirculation generated at the motor head end, propellant mixing is strongly promoted, and combustion takes place in the recirculation core; hot combustion gases are transported from the grain entrance region back to the prechamber, where temperature is very high. Downstream of the recirculation, the temperature distribution reflects the typical structure of a diffusion flame, with a narrow region close to the fuel surface where the near-stoichiometric conditions are reached and the temperature shows its maximum value. Anyway, as a consequence of the relatively high turbulent kinetic energy determined by the different vortices, relatively high temperatures characterize also the core flow.

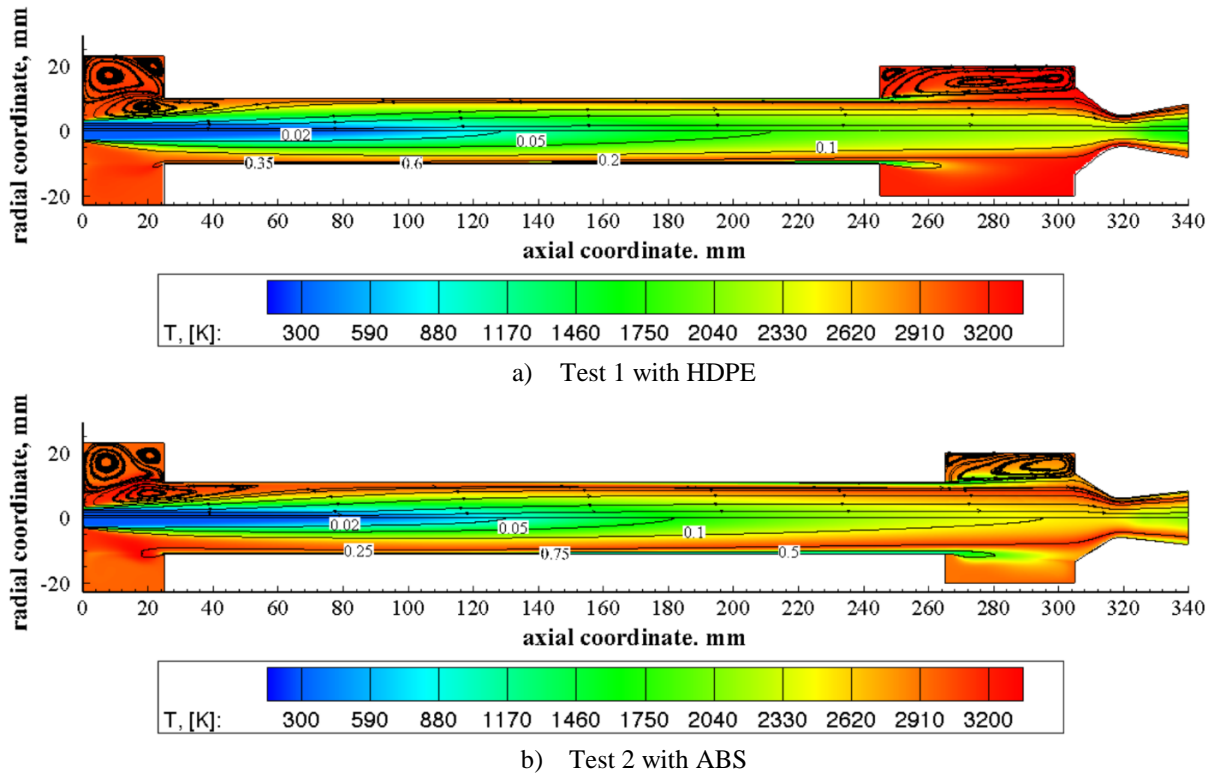


Figure 8: Temperature contour plot with overlapped streamlines (top half) and mixture fraction iso-lines (bottom half)

Figure 9 shows the computed fuel regression rate axial profiles in the two considered cases compared with the experimental data of the corresponding firing tests. In both cases, the regression rate axial distribution yields a peak, due to the oxygen jet impingement, followed by a minimum point, after which it monotonically increases. This behaviour is typical of the boundary layer heat transfer, for which the heat flux increase due to the mass addition down the port becomes dominant on the decrease due to the boundary layer growth from a certain axial distance. Furthermore, this effect is more prominent in the case of the test with ABS, where the fuel regression rate and consequently the mass addition are higher.

Considering that the numerical regression rates have been calculated at the average port diameter, whereas the experimental data are, of course, been retrieved after the motor extinguishment, in both the firing test cases a good agreement between numerical results and experiments is shown, yielding the maximum deviation in correspondence of the point of maximum consumption; however, note that in this zone the maximum experimental uncertainty is obtained, because of the asymmetric consumption determined by the motor ignition device.

The validation of the numerical model is confirmed by the values of the computed averaged pressure in the aft-mixing chamber, reported in Table 5, which again are in good agreement with the corresponding experimentally measured values.

Table 5: Computed average pressure in the aft-mixing chamber and deviation with experimental data

Test case	Computed averaged fuel regression rate (mm/s)	Regression rate relative error	Aft-mixing chamber pressure (atm)	Chamber pressure relative error
HDPE	0.384	1.54%	6.52	1.7%
ABS	0.581	4.75%	4.91	2.7%

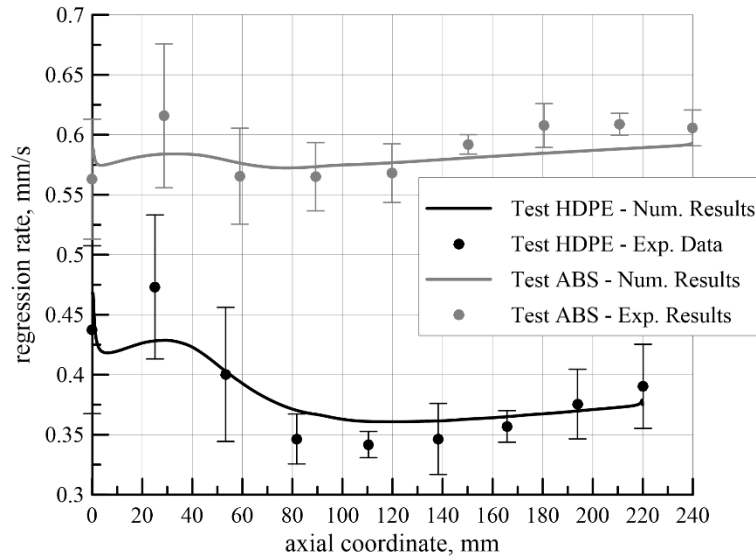


Figure 9: Regression rate distributions evolution in the firing with the axial-nozzle injector

#### 4.2 Numerical simulation of nozzle flow and thermal behaviour

In this section, the results of the numerical simulation of the flow field through the discharged nozzle and of the unsteady thermal field in the solid are presented.

As mentioned in Sec. 3.2, the simulation was carried out considering as input on the nozzle inlet section the results from the numerical simulation of the hybrid rocket internal ballistics in the case of the test with HDPE. The profiles of the total pressure, total temperature and of the mass fractions of the main chemical species are shown in Figure 10.

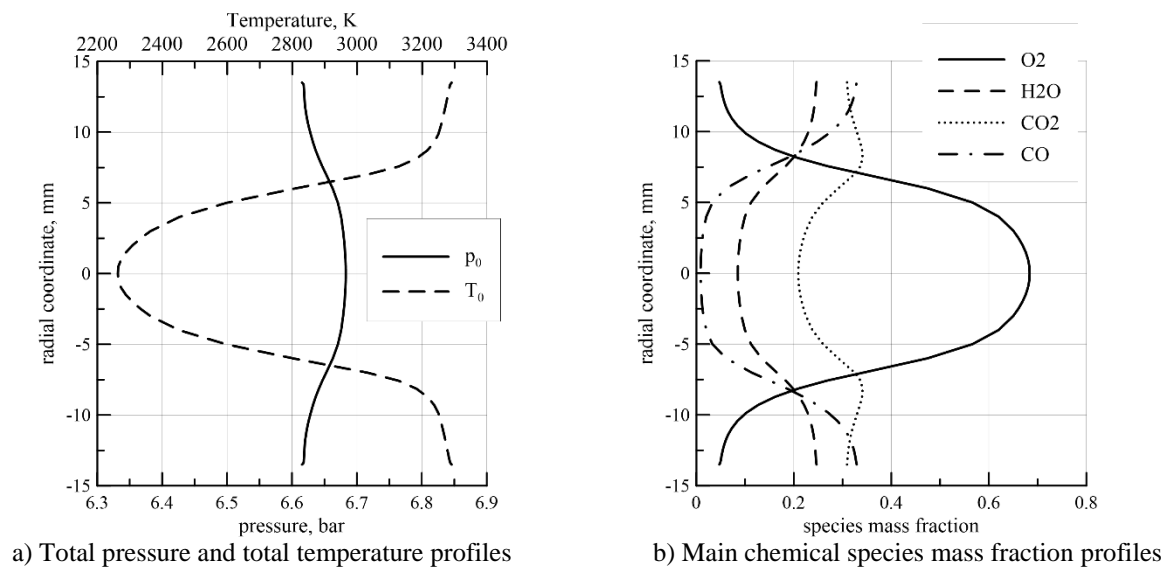


Figure 10: Profiles of flow quantities on the nozzle inlet section

Figure 11 shows the pressure and temperature distributions of the exhaust gases flow through the nozzle. Since the total pressure set at the inlet section is rather uniform, the pressure distribution is typical of the one-dimensional expansion through a converging-diverging duct. On the contrary, the temperature distribution reflects the flame structure coming from the combustion chamber, with higher temperature near the wall and lower temperature in the core flow, coherently with the results shown in Figure 8a.

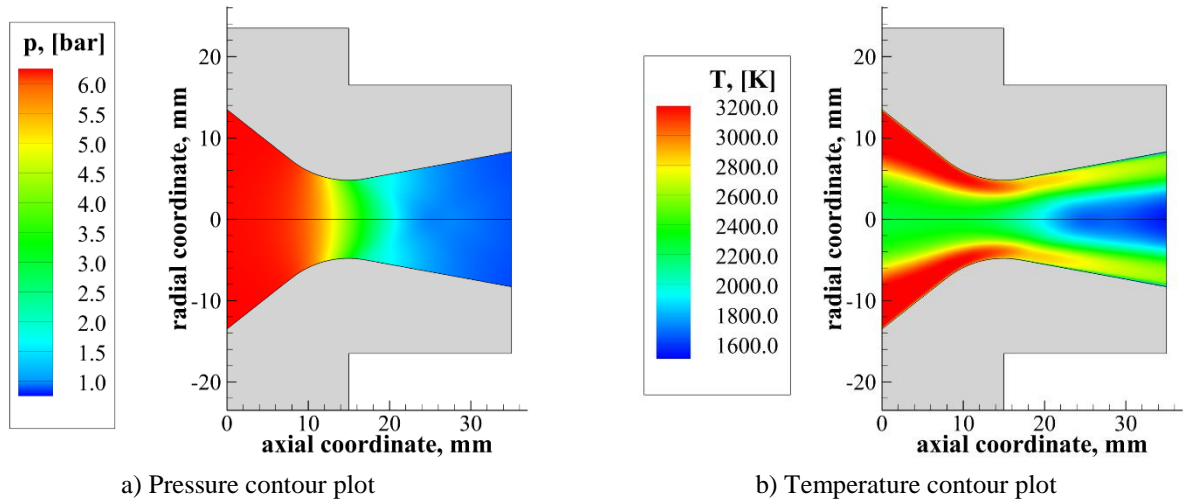
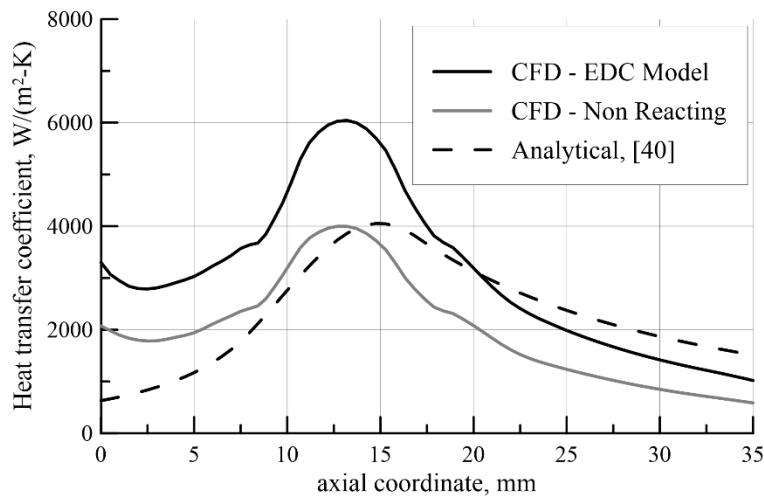


Figure 11: Results of the numerical simulation of the flow field through the discharged nozzle

Figure 12 shows the heat transfer coefficient along the nozzle inner surface, defined as

$$h = \frac{\dot{q}_w}{(T_0 - T_w)} \quad (10)$$

where  $\dot{q}_w$  is the convective heat flux to the wall,  $T_0$  is the average temperature in the nozzle inlet section  $T_w$  is the wall temperature. The curves are estimated for the case of cold wall. The profile obtained with the numerical model described in Section 3.2 is compared with the result of a similar numerical simulation considering frozen chemical composition and with the profile estimated with the well-known analytical method proposed by Bartz [41]. It can be noticed that, according to both the CFD simulations, the maximum heat transfer is reached slightly upstream of the throat section, where, on the other hand, the maximum predicted by the Bartz's relationship is located. Furthermore, the reacting model yields higher values of the heat transfer in the converging part up to the throat section with respect to the other models, which are both based on the hypothesis of frozen chemical composition. This may be explained by the fact that in the converging portion of the nozzle the chemical reaction characteristic time is still comparable with the convection characteristic time, due to the relatively small velocities and high temperature. Consequently, the recombination reactions play an important role and determine higher flame temperatures and corresponding higher heat fluxes. On the other hand, in the diverging portion of the nozzle, where the convection characteristic time becomes lower than the chemical kinetics one, there is a better agreement between the profiles predicted by the different methods.

Figure 12: Heat transfer coefficient along the nozzle inner surface for cold wall ( $T_w = 300K$ )

As mentioned before, the CFD model including the chemical reactions has been employed for the following analyses. Figure 13 shows the total heat flux profile along the nozzle inner surface for cold wall, which takes into account also the radiative contribution. Of course, the profile has the same trend above described for the heat transfer coefficient. At the beginning of the test, very high values of the heat flux are predicted up to 18 MW/m<sup>2</sup>.

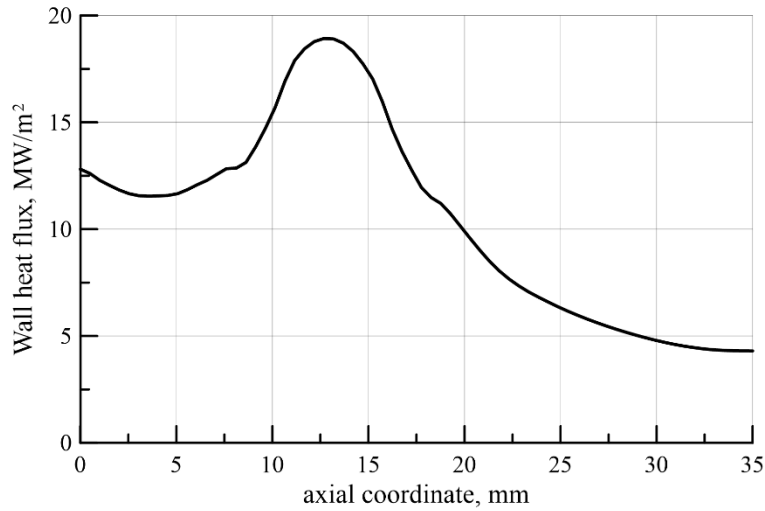


Figure 13: Total heat flux along the nozzle inner surface for cold wall ( $T_w = 300K$ )

The flowfield solution has been then coupled with the thermal analysis of the solid nozzle. Two different cases have been considered: first, a graphite nozzle, and, second, a typical ceramic material (namely with higher density and lower thermal conductivity) have been analysed. The thermal properties considered in the two cases are reported in Table 6.

Table 6: Properties of the solid materials

Material	Density [kg/m <sup>3</sup> ]	Thermal conductivity [W/(m K)]	Specific heat [J/(kg K)]	Surface emissivity
Graphite	1800	104	710	0.75
Ceramic	3210	10	750	0.8

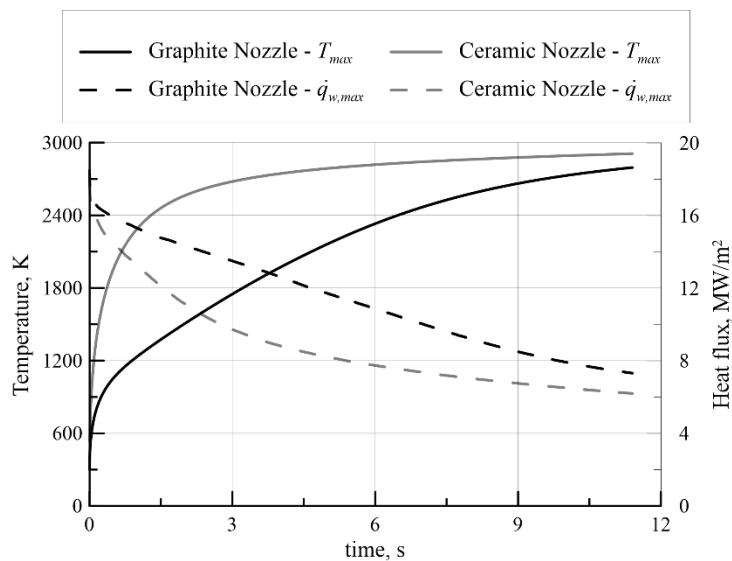


Figure 14: Maximum temperature and heat flux on the nozzle inner surface vs time.

Figure 14 shows the temporal profiles of the maximum values of the temperature and the surface heat flux for the two considered cases. It can be noticed that, in the case of graphite nozzle, after the early instants, temperature increases and the heat flux correspondingly decreases smoothly; whereas in the case of the ceramic nozzle, because of both the higher density and mainly the lower thermal conductivity, the variation of both temperature and heat flux is very steep in the first two seconds.

The different behaviour of the two nozzle materials can be seen also by the temperature distribution in the solid region, shown in Figure 15, calculated at the final instant of the burn of the test with HDPE (see Figure 4). In fact, in the case of graphite nozzle, relatively high temperature occurs in the whole solid region, with a difference of only around 600 K between the maximum value, reached around the nozzle throat, and the minimum value, reached on the backward external surface. On the other side, in the case of ceramic nozzle, large temperatures are rapidly reached on the internal surface, whereas the external region remains relatively cold for the entire firing duration, determining severe temperature gradients.

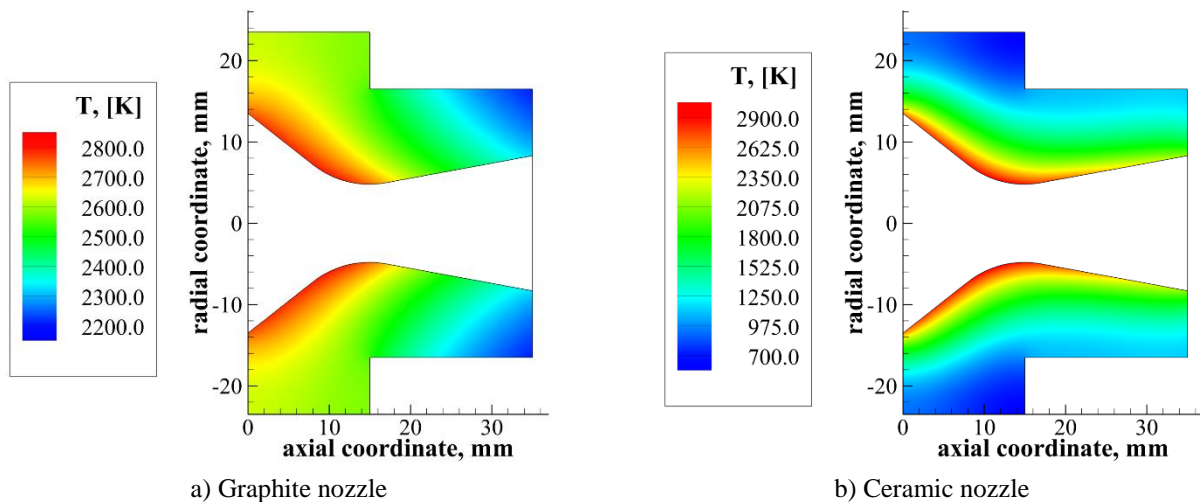


Figure 15: Temperature distribution in the solid nozzle at the end time ( $t = 11.4s$ )

## 5. Conclusions

A CFD approach to the internal ballistics of hybrid rocket engines with integrated gas/surface interaction modelling for the prediction of the fuel regression rate has been presented. The Reynolds-averaged Navier–Stokes equations, with two additional transport equations for the average mixture fraction and its variance combined to the probability density function combustion model and thermochemical equilibrium are solved, coupled with a suitable sub-model to describe the fuel pyrolysis and regression, based on the local mass, energy and mixture fraction balance. Two test cases, represented by the combustion in a laboratory small scale hybrid rocket burning gaseous oxygen with either HDPE or ABS fuel grain have been simulated. In both cases, the model has been demonstrated to capture the fundamental features of the motor internal ballistics, which involve recirculation at the grain port inlet with the characteristic heat transfer mechanism leading to a point of maximum regression rate, not only from a qualitative standpoint. The numerical results compared to the fuel regression rate experimental data show a fair agreement, as well as the comparison between the calculated and the measured chamber pressures.

Results of the numerical simulation carried out in the test case with HDPE have been used as input to the combined simulation of the gaseous flow through the nozzle coupled to the unsteady thermal field in the solid component; two cases of a graphite nozzle and of a ceramic nozzle have been analysed. Because of the lower thermal conductivity, in the latter case the component is subjected to high temperatures and severe temperature gradients. Future numerical and experimental studies are foreseen to validate the numerical model employed and to confirm the expected behaviour.

## Acknowledgements

This project has received funding by the European Union's Horizon2020 research and innovation programme under the Grant Agreement 685594.

## References

- [1] Marxman, G. A., and M. Gilbert. 1963. Turbulent Boundary Layer Combustion in the Hybrid Rocket. In: *Ninth International Symposium on Combustion*. 371-383.
- [2] Carmicino, C., and A. Russo Sorge. 2005. Role of Injection in Hybrid Rockets Regression Rate Behavior. *J. Propuls. Power*. 21:606-612.
- [3] Bianchi, D., B. Betti, F. Nasuti, and C. Carmicino. 2015. Simulation of Gaseous Oxygen/Hydroxyl-Terminated Polybutadiene Hybrid Rocket Flowfields and Comparison with Experiments. *J. Propuls. Power*. 31:919-929.
- [4] Savino, R., G. Festa, A. Cecere, L. Pienti, and D. Sciti. 2015. Experimental Set Up for Characterization of Carbide-Based Materials in Propulsion Environment. *J. Eur. Ceram. Soc.* 35:1715-1723.
- [5] Silvestroni, L., and D. Sciti. 2011. Ultra-high temperature ceramics reinforced with SiC short fiber or whisker. in *Fiber-Reinforced Composites*, Ed. by F Columbus, Nova Science Publishers, Inc, Hauppauge, NY, (Chapter 11).
- [6] Sankaran, V. 2007. Computational Fluid Dynamics Modeling of Hybrid Rocket Flowfields. In: *Fundamentals of Hybrid Rocket Combustion and Propulsion*, edited by K. Kuo, M. Chiaverini, Vol. 218, Progress in Astronautics and Aeronautics, AIAA. 323-349.
- [7] Kumar, C. P., and A. Kumar. 2013. Effect of Diaphragms on Regression Rate in Hybrid Rocket Motors *J. Propuls. Power*. 29:559-572.
- [8] Chen, Y. S., T. H. Chou, B. R. Gu, J. S. Wu, B. Wu, Y. Y. Lian, and L. Yang. 2011. Multiphysics Simulations of Rocket Engine Combustion. *Comput. Fluids*. 45:pp. 29-36.
- [9] Coronetti, A., and W. A. Sirignano. 2013. Numerical Analysis of Hybrid Rocket Combustion. *J. Propuls. Power*. 29:371-384.
- [10] Lazzarin, M., F. Barato, A. Bettella, and D. Pavarin. 2013. Computational Fluid Dynamics Simulation of Regression Rate in Hybrid Rockets. *J. Propuls. Power*. 29:1445-1452.
- [11] Kim, B., Y. Na, K. Shin, and C. Lee. 2012. Nonlinear Combustion and Fluid Mechanics in a Hybrid Rocket. *J. Propuls. Power*. 28:1351-1358.
- [12] Lengellé, G., 2007. Solid-Fuel Pyrolysis Phenomena and Regression Rate, Part 1: Mechanisms. In: *Fundamentals of Hybrid Rocket Combustion and Propulsion*, edited by K. Kuo, M. Chiaverini, Vol. 218, Progress in Astronautics and Aeronautics, AIAA. 127-163.
- [13] Motoe, M., and T. Shimada. 2014. Numerical Simulations of Combustive Flows in a Swirling-Oxidizer-Flow-Type Hybrid Rocket. *52nd Aerospace Sciences Meeting*. No. 2014-0310.
- [14] Bianchi, D., and F. Nasuti. 2013. Numerical Analysis of Nozzle Material Thermochemical Erosion in Hybrid Rocket Engines. *J. Propuls. Power*. 29:547-558.
- [15] Leccese, G., D. Bianchi, and F. Nasuti. 2016. Simulations of Hybrid Rocket Flowfields Including Modeling of Fuel Pyrolysis and Thermal Radiation. *5th Space Propulsion Conference*. SP2016-3125176.
- [16] Di Martino, G. D., P. Malgieri, C. Carmicino, and R. Savino. 2016. A Simplified Computational Fluid-Dynamic Approach to the Oxidizer Injector Design in Hybrid Rockets. *Acta Astronaut.* 129:8-21.
- [17] Di Martino, G. D., C. Carmicino, and R. Savino. 2017. Transient Computational Thermofluid-Dynamic Simulation of Hybrid Rocket Internal Ballistics. *J. Propuls. Power*.
- [18] Carmicino, C., F. Scaramuzzino, and A. Russo Sorge. 2014. Trade-off Between Paraffin-Based and Aluminium-Loaded HTPB Fuels to Improve Performance of Hybrid Rocket fed with N<sub>2</sub>O. *Aerosp. Sci. Technol.* 37:81-92.
- [19] Carmicino, C. 2009. Acoustics, Vortex Shedding, and Low-Frequency Dynamics Interaction in an Unstable Hybrid Rocket. *J. Propuls. Power*. 25:1322-1335.
- [20] Russo Sorge, A., C. Carmicino, and A. Nocito. 2002. Design of a Lab-scale Cooled Two-dimensional Plug Nozzle for Experimental Tests. AIAA paper No. 2002-4039.
- [21] Bonifacio, S., G. Festa, and A. Russo Sorge. 2013. Novel Structured Catalysts for Hydrogen Peroxide Decomposition in Monopropellant and Hybrid Rockets. *J. Propuls. Power*. 29:1130-1137.
- [22] Galfetti, L., F. Nasuti, D. Pastrone, and A.M. Russo. 2014. An Italian Network to Improve Hybrid Rocket Performance: Strategy and Results. *Acta Astronaut.* 96:246-260.
- [23] Carmicino, C. and A. Russo Sorge. 2015. Experimental Investigation into the Effect of Solid-Fuel Additives on Hybrid Rocket Performance. *J. Propuls. Power*. 31:699-713.
- [24] Chorin, A. J. 1968. Numerical Solution of Navier-Stokes Equations. *Math. of Comput.* 22:745-762.
- [25] Menter, F.R., 1994. Two-Equation Eddy-Viscosity Turbulence Models for Engineering Applications. *AIAA J.* 32:1598-1605.
- [26] Wilcox, D.C., 1998. Turbulence Energy Equation Models. *Turbulence Modeling for CFD*, DCW Industries, Inc. La Canada. 73-170.
- [27] Wooldridge, C. E., G. A. Marxman, and R. J. Kier. 1969. Investigation of Combustion Instability in Hybrid Rockets. NASA contract NAS 1-7310, Stanford Research Inst.
- [28] Sivathanu, Y. R., and G. M. Faeth. 1990. Generalized State Relationships for Scalar Properties in Non-Premixed Hydrocarbon/Air Flames. *Combust. Flame*. 82:211-230.

- [29] Hazewinkel, M. 2001. Beta-distribution”, Encyclopedia of Mathematics, Springer, 2001, ISBN 978-1-55608-010-4
- [30] Gordon, S., B. J. McBride. 1994. Computer Program of Complex Chemical Equilibrium Compositions and Applications. NASA Reference Publication 1311.
- [31] Whitmore, S. A., Z. W. Peterson and S. D. Eilers. 2011. Analytical and Experimental Comparison of HTPB and ABS as Hybrid Rocket Fuels. AIAA Paper No. 2011-5909.
- [32] Chiaverini, M. 2007. Review of Solid Fuel Regression. In: *Fundamentals of Hybrid Rocket Combustion and Propulsion*, edited by Kuo, K., and Chiaverini, M., Progress in Astronautics and Aeronautics, Vol. 218, AIAA. 49–93.
- [33] de Wilde, J. P., 1988. The Heat of Gasification of Polyethylene and Polymethylmethacrylate. Rept. PML 1988-C42, `SFCC Publ. 53, Faculty of Aerospace Engineering/Prins Maurits Lab./Solid Fuel Combustion Chamber, Delft Univ. of Technology, Delft, The Netherlands.
- [34] Karabeyoglu, A., B. J. Cantwell, and J. Stevens. 2005. Evaluation of Homologous Series of Normal-Alkanes as Hybrid Rocket Fuels. AIAA Paper No. 2005-3908.
- [35] Whitmore, S. A., J. R. Wilson, M. A. Ritter, and L. T. Williams. 2015. Estimating the Enthalpy of Gasification of Acrylonitrile-Butadiene-Styrene Hybrid Rocket Fuels. *J. Propuls. Power.* 31:1033–1040.
- [36] Magnussen, B.F. 1981. On the Structure of Turbulence and a Generalized Eddy Dissipation Concept for Chemical Reaction in Turbulent Flow. In: *Nineteenth AIAA Meeting*.
- [37] Singh, D. J., and C. J. Jachimowski. 1994. Quasiglobal Reaction Model for Ethylene Combustion. *AIAA J.* 32:213-216.
- [38] Modest, M. F. 2003. Radiative Heat Transfer 2nd Edition. Academic Press. New York.
- [39] Carmicino, C., and A. Russo Sorge. 2006. The Effects of Oxidizer Injector Design on Hybrid Rockets Combustion Stability, AIAA Paper No. 2006-4677.
- [40] Pastrone, D., L. Casalino, and C. Carmicino. 2014. Analysis of Acoustics and Vortex Shedding Interactions in Hybrid Rocket Motors. *J. Propuls. Power.* 30: 1613-1619.
- [41] Bartz D. R. 1965. Turbulent boundary-layer heat transfer from rapidly accelerating flow of rocket combustion gases and of heated air. *Adv. Heat Transf.* 2:1-108.